Accelerating and Supersonic Density Fluctuations in Coronal Hole Plumes: Signature of Nascent Solar Winds

Il-Hyun Cho[1] , Valery M. Nakariakov[2,3,4] , Yong-Jae Moon[1,3] , Jin-Yi Lee[1] , Dae Jung Yu[3] , Kyung-Suk Cho[5,6] ,
Vasyl Yurchyshyn[7] , and Harim Lee[1]

[1] Department of Astronomy and Space Science, Kyung Hee University, Yongin, 17104, Republic of Korea; moonyj@khu.ac.kr
[2] Centre for Fusion, Space and Astrophysics, Department of Physics, University of Warwick, Coventry CV4 7AL, UK
[3] School of Space Research, Kyung Hee University, Yongin, 17104, Republic of Korea
[4] Special Astrophysical Observatory, Russian Academy of Sciences, St. Petersburg, 196140, Russia
[5] Space Science Division, Korea Astronomy and Space Science Institute, Daejeon, 34055, Republic of Korea
[6] Department of Astronomy and Space Science, University of Science and Technology, Daejeon, 34055, Republic of Korea
[7] Big Bear Solar Observatory, New Jersey Institute of Technology, 40386 North Shore Lane, Big Bear City, CA 92314-9672, USA
Received 2020 July 30; revised 2020 August 13; accepted 2020 August 17; published 2020 September 3

Abstract

Slow magnetoacoustic waves in a static background provide a seismological tool to probe the solar atmosphere in the analytic frame. By analyzing the spatiotemporal variation of the electron number density of plume structure in coronal holes above the limb for a given temperature, we find that the density perturbations accelerate with supersonic speeds in the distance range from 1.02 to 1.23 solar radii. We interpret them as slow magnetoacoustic waves propagating at about the sound speed with accelerating subsonic flows. The average sonic height of the subsonic flows is calculated to be 1.27 solar radii. The mass flux of the subsonic flows is estimated to be 44.1% relative to the global solar wind. Hence, the subsonic flow is likely to be the nascent solar wind. In other words, the evolution of the nascent solar wind in plumes at the low corona is quantified for the first time from imaging observations. Based on the interpretation, propagating density perturbations present in plumes could be used as a seismological probe of the gradually accelerating solar wind.

Unified Astronomy Thesaurus concepts: Solar coronal plumes (2039); Solar coronal seismology (1994); Solar wind (1534)

1. Introduction

Slow magnetoacoustic waves are a useful seismological tool to probe the solar atmosphere (e.g., Cho et al. 2017, 2019). MHD waves propagating in a flowing background with a constant speed are faster than phase speeds of the waves in a static medium due to the Doppler effect, which was predicted by theories (Goossens et al. 1992; Nakariakov et al. 1996) and observations (Chen et al. 2011; Feng et al. 2011; Decraemer et al. 2020). A wave propagation in a flowing background with a nonconstant speed may not be analyzed analytically, but can be explored in a simulation (Griton et al. 2020).

Solar plumes are thin and ray-like structures rooted above networks and extended up to at least 30 solar radii (Deforest et al. 1997; DeForest et al. 2001). Plumes are known to be cooler and denser than their surrounding interplumes (Poletto 2015). It was found that a plume in extreme ultraviolet (EUV) bands disappears due to a density reduction rather than temperature decrease (Pucci et al. 2014). It was also found that EUV intensities are enhanced above the enhanced spicular activity (Samanta et al. 2019). These structures are thought to be magnetic tubes that guide MHD waves (Nakariakov 2006; Banerjee et al. 2011; Poletto 2015) that were observed as periodically propagating intensity disturbances in various wavelength bands (Ofman et al. 1997, 1999; DeForest & Gurman 1998; Wang et al. 2009; Gupta et al. 2010; Krishna Prasad et al. 2011; Gupta et al. 2012; Krishna Prasad et al. 2014, 2018), and/or mass-flows (McIntosh et al. 2010; Tian et al. 2011; Pucci et al. 2014).

In this study, we provide evidence of wave propagations in an accelerating background with a subsonic speed in plume structures. For this, a propagation speed of density fluctuations in plume structures is estimated and compared with the sound speed obtained from the electron temperature given by the differential emission measure (DEM). In Section 2, we describe data and method to distinguish the plume structures in a plume line of sight (LOS). In Section 3, we perform the least-squares fitting to the evolution of density fluctuation by the second-order polynomial and explore the property of background flow. Finally, we summarize and discuss our results.

2. Data and Method

2.1. Plume Structures in the Plume LOS

We use narrowband filtergram images at 94, 131, 171, 193, 211, and 335 Å taken by the Atmospheric Imaging Assembly (AIA; Lemen et al. 2012) on board the Solar Dynamics Observatory (SDO; Pesnell et al. 2012) on 2017 January 3 00:00 UT–24:00 UT. During the observation day, the entire Sun was very quiet. Each image is rotated based on the solar P angle and resized to have a pixel resolution of $0\overset{''}{.}600$ at a distance of 1.496×10^8 km, which is the reference distance given in data. The intensity is scaled according to the changes in pixel resolution and the disk size.

Plumes are embedded in interplume background. To minimize the effects from interplume emission on the estimation of the density and temperature, we define the plume LOS and interplume LOS separately, as in Figure 1. We define slits that indicate the boundaries of plume and interplume LOSs based on the 1 day averaged intensity of the AIA 171 Å band (Figure 1(c)). The slits on the intensity images for the other five bands are the same with that of the intensity image of 171 Å. The plume was inclined to ∼4° relative to the direction normal
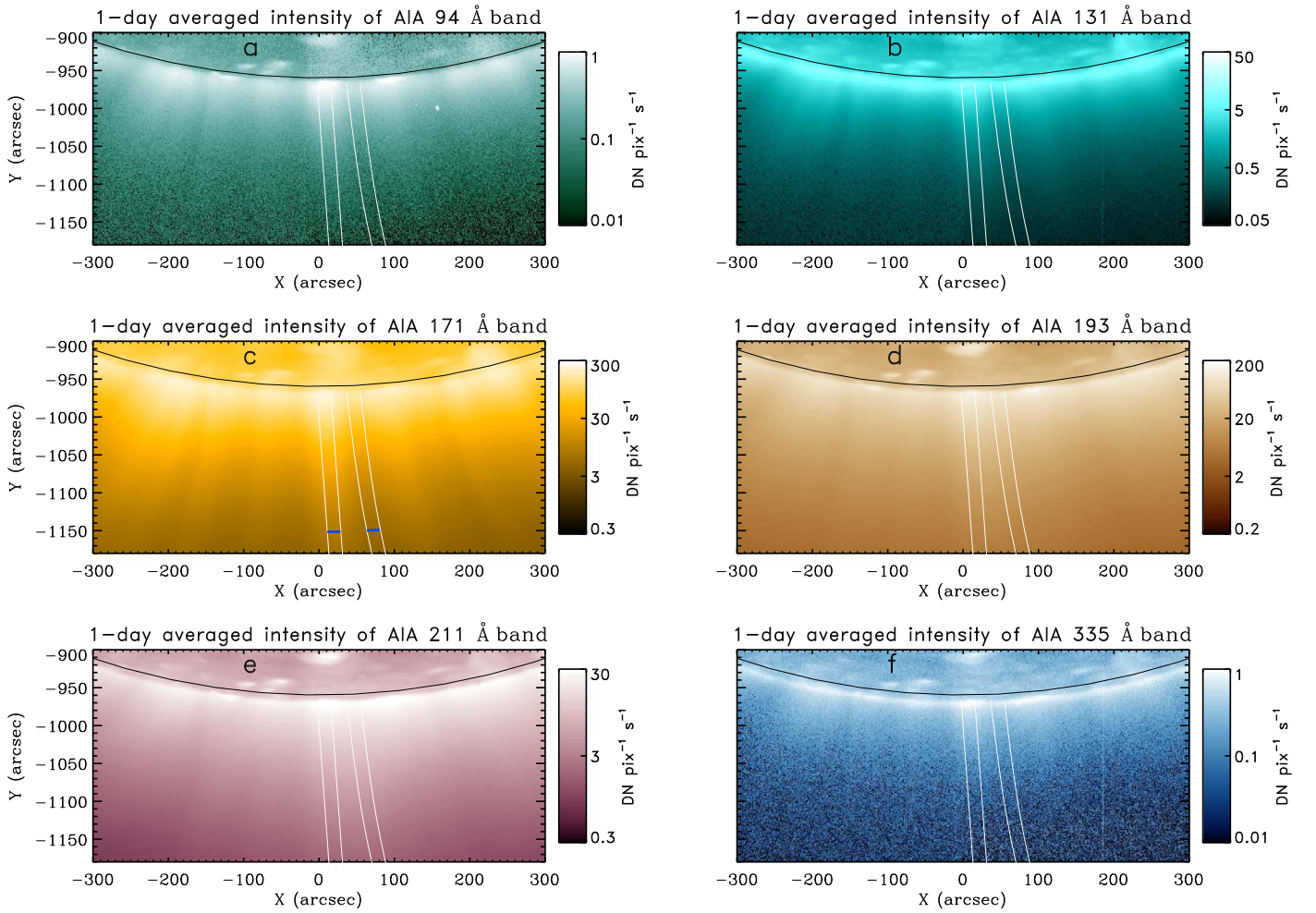
Figure 1. One-day averaged intensities of 94, 131, 171, 193, 211, and 335 Å bands taken by the SDO/AIA for the south polar region (a)–(f). Two white lines on the left and right in each panel are boundaries of plume LOS and interplume LOS. From these regions, intensities for plume and interplume LOSs are constructed as a function of heliocentric distance and time. The blue horizontal lines indicate the height of 1.2 solar radii.

to the solar surface. The interplume was also inclined, but the axis looks to be curved. Both the positions of straight and curved lines are determined by first- and second- order polynomial fittings from several locations that were visually determined. Along the slits, the intensities of the (inter)plume LOS between boundaries at the (right) left are averaged for a given height and frame. For example, the average intensity of the 171 Å band on the plume LOS at a distance of 1.2 solar radii is determined from intensities along the positions indicated by the blue line on the left in Figure 1(c), and that on the interplume is from the positions indicated by the blue line on the right. Note that slit distances in the plume and interplume LOSs are different from each other at a given height. The distance in our study represents the heliocentric distance corresponding to the inclined slit distance of the plume LOS.

2.2. Differential Emission Measure

The DEM represents the amount of emission of plasma, and gives an electron number density for a given temperature and length of the LOS. The intensity of the filtergram with narrow ranges of wavelength on EUV taken by the SDO/AIA (I_i) can be modeled as $\int_T R_i(T) \mathrm{DEM}(T) dT$, where I_i and R_i represent intensity and temperature response for a certain channel.

Temperature response functions are slightly different for different abundances (e.g., Lee et al. 2017). It is likely that abundance enhancements are not able to be built up in an open magnetic field structure of coronal holes. Hence, we use the photospheric abundance (Caffau et al. 2011) that gives the temperature response of 171 Å at around 0.8 MK to be ∼2 times lower compared to that from the conventional coronal one (Feldman 1992).

To derive the DEM, we apply the recently developed method, the Solar Iterative Temperature Emission Solver (SITES; Morgan & Pickering 2019) for a given pixel on the time–distance images constructed on the plume LOS and the interplume LOS. The method calculates a DEM directly from the observed intensities and fractional temperature response functions. As a result, we obtain DEM $_{\mathrm{Plume\ LOS}}(t, h, T)$ and DEM $_{\mathrm{Interplume\ LOS}}(t, h, T)$, where t, h, and T are the time, height, and temperature bin, respectively. DEMs are 1 minute averaged to enhance the signal-to-noise ratios. From this, we define the DEM of plume structures $\mathrm{DEM}_{\mathrm{Plume}}$ as $\mathrm{DEM}_{\mathrm{Plume\ LOS}} - \mathrm{DEM}_{\mathrm{Interplume\ LOS}}$. A snapshot of $\mathrm{DEM}_{\mathrm{Plume\ LOS}}$, $\mathrm{DEM}_{\mathrm{Interplume\ LOS}}$, and $\mathrm{DEM}_{\mathrm{Plume}}$ are presented in Figures 2(a) and (b), which are taken from the position indicated by the cross in Figure 2(c). As shown in Figure 2(a), both DEMs have two bumps at around 0.8 and 2 MK, but the latter bumps are identical in both LOSs. It was found that the
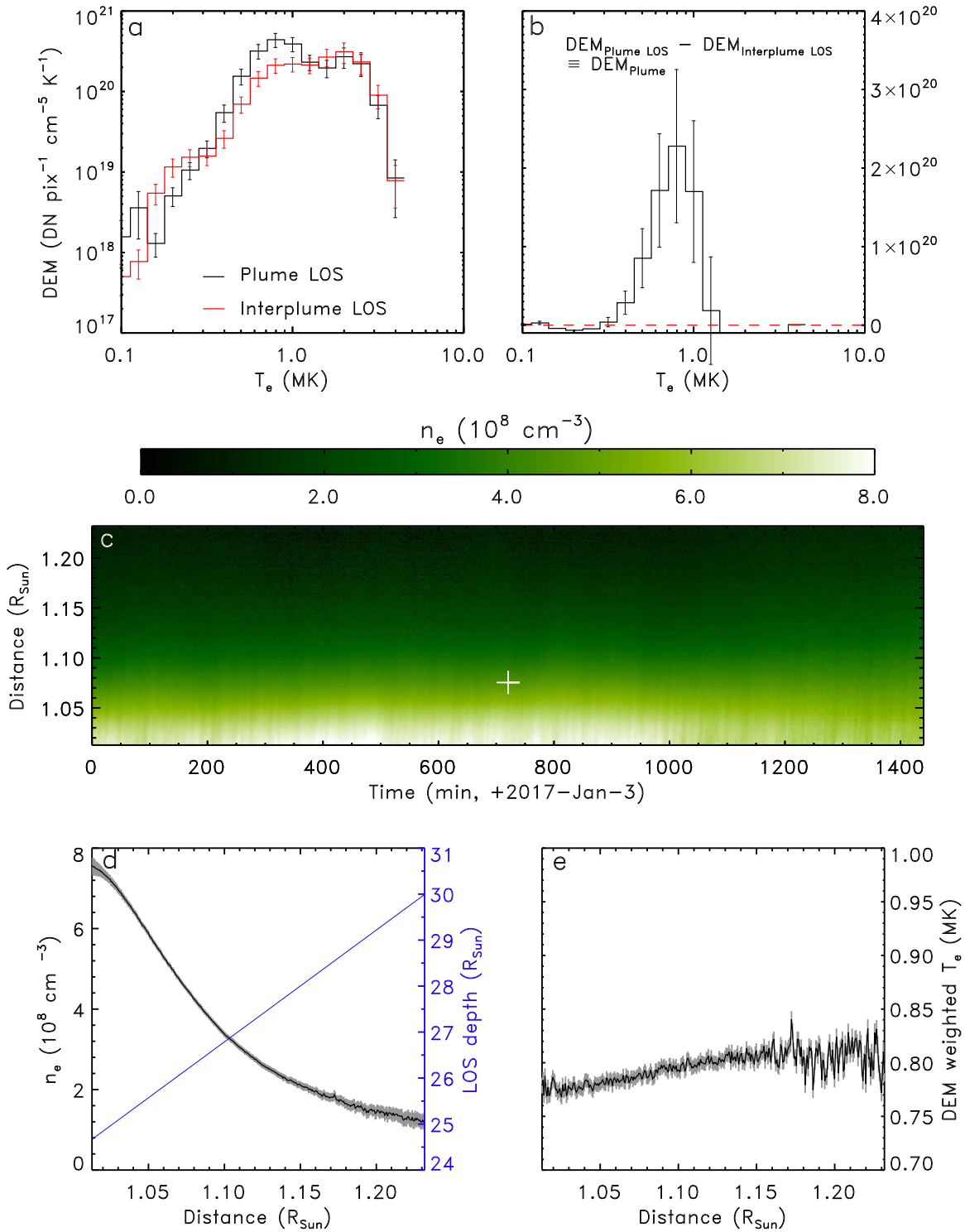
Figure 2. Examples of DEMs for plume LOS (black) and interplume LOS (red) at an arbitrary time and distance (a), their difference (b), the map of electron number density (c), and temporal averages of the electron number density and temperature as a function of distance (d), (e). The vertical bars in panel (a) represent $\pm 1\sigma_{\mathrm{DEM_{Plume\,LOS}}}$ and $\pm 1\sigma_{\mathrm{DEM_{Interplume\,LOS}}}$. The vertical bars in panel (b) represent $\pm 1\sigma_{\Delta \mathrm{DEM}}$ defined by $\sqrt{\sigma_{\mathrm{DEM_{Plume\,LOS}}}^2 + \sigma_{\mathrm{DEM_{Interplume\,LOS}}}^2}$. The red dashed line in panel (b) indicates the zero DEM. The gray area in panels (d) and (e) represent $\pm 1\sigma_{n_e}$ and $\pm 1\sigma_{T_e}$. The blue solid line in panel (d) is the diameter of a single plume.

temperature of the equatorial coronal holes is $\sim$0.9 MK, but becomes higher if the region of interest includes outer quiet regions (Saqri et al. 2020). The off-limb measurement certainly includes emissions from the quiet region at different heights. Hence, we believe that the temperature of former bumps is likely to be the typical value of the plume in coronal holes. This result is well explained with an assumption when both the

plume and interplume LOSs include plume structures and $\sim$2 MK backgrounds, then the interplume LOS includes fewer plume structures. Hence, the subtraction of $\mathrm{DEM_{Interplume\,LOS}}$ from $\mathrm{DEM_{Plume}}$ can minimize a contribution to plume emissions from the background, but also reduces emissions from plumes along the plume LOS.

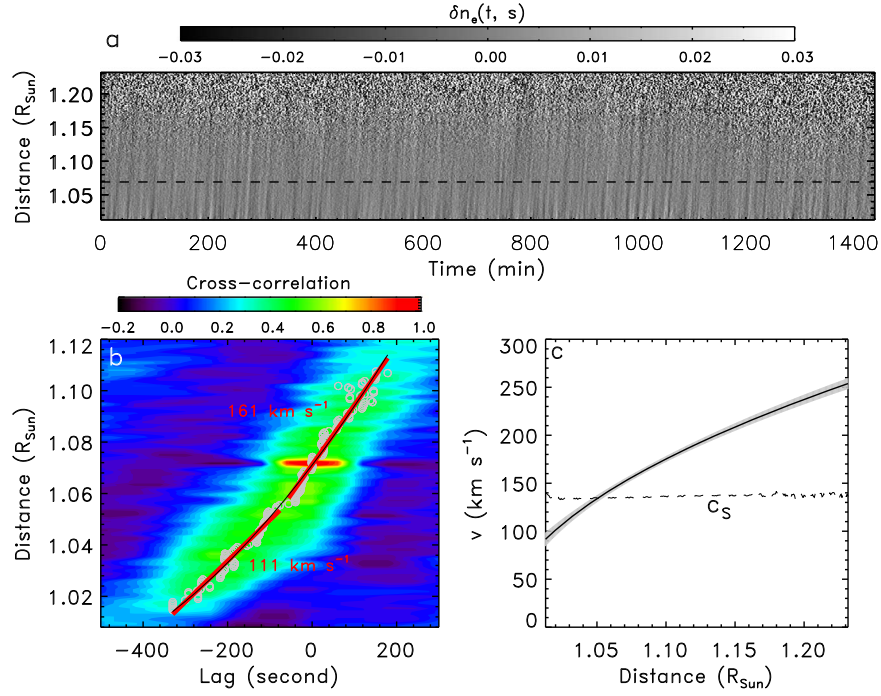**Figure 3.** Perturbations of electron number density ($\delta n_e \equiv d(n_e/<n_e>_t - 1)$) as a function of time and heliocentric distance (a), the average cross-correlations obtained from 95 sub-images, as a function of lag and distance (b), and the average speed of the density perturbations as a function of distance (c). In panel (b), the gray circle indicates the weighted mean of the correlation for a given distance. Two red solid lines represent the linear least-squares fits for the distances as a function of lags. The thin black solid line is the second-order polynomial fit. In panel (c), the speed and its range of error are represented by the black and gray colors. The dashed line represents the sound speed calculated from the temporally averaged temperature for a given distance (see Figure 2(e)).

The emission measure, $\mathrm{EM}_{\mathrm{Plume}}(t, h)$, is defined as $\int_T \mathrm{DEM}_{\mathrm{Plume}}(t, h, T)dT$. The electron number density, $n_e(t, h)$, is defined as $\sqrt{\frac{\mathrm{EM}_{\mathrm{Plume}}(t, h)}{dl(h)}}$, and presented in Figure 2(c). The LOS length of plumes, $dl(h)$, is set to be the length of chord ($2h\tan\theta$) for a single plume, where h is the height, θ is half of the angular width of a plume ($1°$), which corresponds to 24–30 Mm. The calculated number density seems to be consistent with the measurement from on-disk coronal holes (Saqri et al. 2020). The electron temperature, $T_e(t, h)$, is defined as $\frac{\int_T \mathrm{DEM}_{\mathrm{Plume}} T dT}{\int_T \mathrm{DEM}_{\mathrm{Plume}} dT}$. The temporal averages of n_e and T_e for a given distance are presented in Figures 2(d) and (e). These quantities are used for the estimation of the mass flux and sound speed.

3. Results

3.1. Evolution of Propagating Density Disturbances

We analyze $\delta n_e(t, h)$ defined by the electron number density (n_e) sequentially subtracted by the previous one, for a given height (Figure 3(a)). We perform the median smoothing with 3 minutes by 3 pixels ($\sim$1.3 Mm) to suppress short-term fluctuations. By visual inspection, there are many propagating quasi-periodic density perturbations during 1 day. We divide the time–distance image into 95 sub-images every 15 minutes having a temporal range $\pm$15 minutes (31 minutes). For each sub-image, we calculate the lagged cross-correlations between the profile at the distance of 50 Mm and profiles for different distances. The average cross-correlation is presented in Figure 3(b). The positive and negative lags represent that the profiles at different distances lead and trail the profile at a distance of 50 Mm, respectively; hence, the migration of the lag

showing maximum correlations from negative to positive indicates the upward propagation.

In Figure 3(b), we plot the weighted-mean lag for a given distance (gray circle). It is clearly shown that the instantaneous slopes of distance evolution ($h(t)$) are different from different times (see the red solid lines). We perform the linear least-squares fittings for the distances at low and high altitudes, and found that the speeds are $111\,\mathrm{km\,s^{-1}}$ and $161\,\mathrm{km\,s^{-1}}$, respectively. Hence, $h(t)$ is likely to accelerate. To quantify the evolution, $h(t)$ was fitted with the second-order polynomial as a function of lag time. As a result, the evolution of the propagation of perturbations is described by a constant acceleration model. The acceleration (a) is calculated to be $183 \pm 12\,\mathrm{m\,s^{-2}}$. The initial speed ($v_0$) at zero height ($h_0$) is found to be $67\,\mathrm{km\,s^{-1}}$.

In Figure 3(c), we plot the fitted speed (v) as a function of distance together with the sound speed (c_S). The speed is given by $\sqrt{v_0^2 + 2a(h - h_0)}$ and its error $\sqrt{v_0^2 \delta v_0^2 + (h - h_0)^2 \delta a^2 + \frac{a^2(\delta h^2 + \delta h_0^2)}{v_0^2 + 2a(h - h_0)}}$, where δv_0, δa, and δh_0 are the errors of the fitting parameters, and δh is taken to be the standard deviation of residuals between h and the observed distance. The speed is compared with the sound speed, which could be the propagation speed of slow magnetoacoustic waves in a static medium of low plasma-β. The sound speed (c_S) is $\sqrt{\frac{\gamma k_B T}{\mu m_H}}$, and equivalent to $90.9 \sqrt{\frac{\gamma < T_e(t, h) >_{1\,\mathrm{MK}}}{\mu}}$ $\mathrm{km\,s^{-1}}$, where $<T_e(t, h)>_{1\,\mathrm{MK}}$ is the temporal average of temperature divided by 1 MK for a given distance as shown in Figure 2(e), $\gamma (=1.67)$ is the adiabatic index, k_B is the Boltzmann constant, m_H is the proton mass, and $\mu (=0.6)$ is the mean molecular weight. It is shown that the speed of the density perturbation becomes faster than the sound speed from $\sim$1.05 solar radii
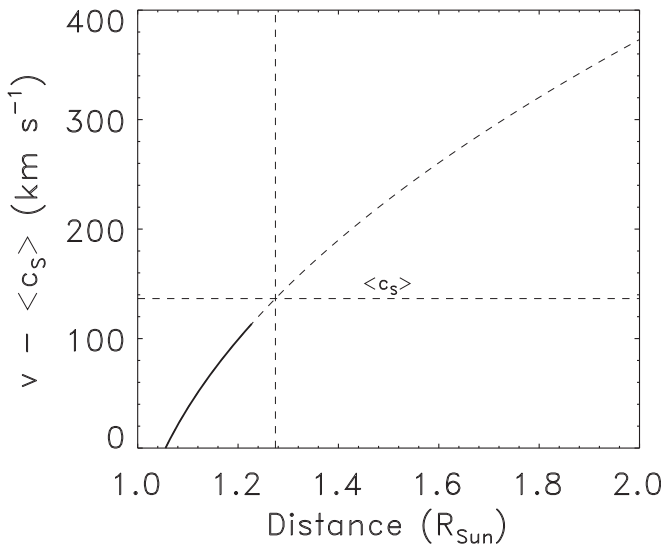
Figure 4. The average speed is extrapolated up to 2 solar radii using the fitting parameters and then subtracted by the mean sound speed, which corresponds to the phase speed of slow waves. The horizontal dashed line indicates the sound speed. The vertical solid line indicates the distance where the extrapolated speed becomes supersonic.

($\sim$35 Mm) and has an excess of $\sim$115 km s^{-1} relative to the sound speed at 1.23 solar radii ($\sim$160 Mm) (see the difference between the black line and dashed line in Figure 3(c)). The excess speed seems to be consistent with radial speeds derived by the Doppler dimming technique (Gabriel et al. 2003; Teriaca et al. 2003). Hence, the excess speed in our study is likely to be the speed of flowing background.

In Figure 4, we present the flow speed defined as the observed speed after subtracting off the mean sound speed, which is assumed to be wave speed. Interestingly, the distance where the flow speed becomes supersonic is $\sim$1.27 solar radii when extrapolated using the fitting parameters. This distance is lower than sonic heights of solar winds (Telloni et al. 2019; Griton et al. 2020). This may be because the extrapolation is based on the constant acceleration motion, which may not adequately describe complex dynamic evolution of solar wind such as deceleration at low altitude (Bemporad 2017).

3.2. Mass Flux

We apply spectral analysis to the density profile at a distance of 50 Mm as indicated in Figure 3(a). We assume that the profile is embedded in red noise because a perturbed medium at a certain time might be influenced by previous perturbations via dissipation or heating. This may result in a frequency-dependent power that is to be an additional noise. A red noise is defined as $\frac{\sigma^2(1-\rho^2)}{\left(1-2\rho\cos\frac{f}{f_N}+\rho^2\right)}$ (Schulz & Mudelsee 2002), where σ is the standard deviation of the density profile in Figure 5(a), ρ is the autoregressive parameter of the autoregressive process of the order 1, f is the frequency (minute^{-1}), and f_N is the Nyquist frequency, respectively. The autoregressive parameter is defined by $e^{-\frac{\Delta t}{\tau_d}}$, where Δt is the sampling interval and τ_d is the decorrelation time that makes the autocorrelation $\frac{1}{e}$ as shown in Figure 5(b). This noise follows the chi-square distribution with two degrees of freedom. It is shown that the Fourier power at 4.8, 5.9, and

8.9 minutes is above the 99% noise level. The observed periods will be used to estimate a temporal filling factor (f_T).

The mass flux is defined as $4\pi d^2\mu m_p n_e v f_T f_{CH} f_S$ (Tian et al. 2014), where d is the heliocentric distance, μ is the mean molecular weight, m_p is the proton mass, n_e is the electron number density, v is the flow speed, f_T is the temporal filling factor, f_{CH} is the fractional area of the coronal hole, and f_S is the spatial filling factor. In Figure 3(b), the perturbation is observed from -300 s to 300 s, hence the lifetime is at least 10 minutes. The temporal filling factor, defined by the ratio of the lifetime ($\sim$10 minutes) to the period (5–9 minutes), could be taken as unity. We use $f_{CH} = 0.05$ and $f_S = 0.1$, indicating that plumes occupy 10% of a coronal hole and the coronal hole covers 5% area of the solar surface. The mass flux is calculated to be 5.6×11^{11} g s^{-1} (8.8×10^{-15} $M_\odot$ yr^{-1}), if we apply $n_e = 2.1 \times 10^8$ cm^{-3} and $v = 66.5$ km s^{-1} at the height of 100 Mm ($d \sim 1.144$ solar radii; see Figures 2(d) and 4). This value corresponds to $\sim$44.1% of the global solar wind (Cohen 2011).

4. Summary and Discussion

In this study, we analyzed the kinematics of perturbations of the electron number density in plume structures above the limb, as a function of time and heliocentric distance, and find that the density perturbations are accelerating up to supersonic speeds for a given temperature. We interpreted them as slow magnetoacoustic waves in a low plasma-β background that is flowing with subsonic speeds and exhibiting acceleration. The acceleration of the subsonic flows is estimated to be 183 ± 12 m^{-2} in the distance range from 1.02 to 1.23 solar radii. The extrapolated sonic height is calculated to be 1.27 solar radii, lower than sonic heights of solar winds ($\sim$2 solar radii; Telloni et al. 2019; Griton et al. 2020). The discrepancy may be explained if solar winds decelerate within $\sim$1.5 solar radii and gently reaccelerate (Bemporad 2017). The mass flux corresponds 44.1% to the global solar wind. Hence, the flowing background is likely to be nascent solar winds.

To our knowledge, this is the first direct measurement of the solar wind speed in plumes from 1.02 to 1.23 solar radii from imaging observations. Our measurement may help to constrain solar wind models at the low corona. A slow wave in an isothermal plume could be used as a seismological probe of the gradually accelerating solar wind. Our observation can support the simulation showing that wave signatures in the presence of solar wind are responsible for propagating intensity features observed in the high corona up to $\sim$30 solar radii (Griton et al. 2020), which were ubiquitously observed in the coronagraphic images (Cho et al. 2018; DeForest et al. 2018).

If the density perturbations are repeated supersonic solar winds, the mass flux corresponds to 134.6% on the global solar wind. The repetition periods are in the narrow range from $\sim$5 to $\sim$9 minutes (Figure 5(c)). Hence, periodic sources are required. If periodic magnetic reconnections are the sources (Samanta et al. 2015), the flow speeds are Alfvénic. However, the observed speed seems to be sub-Alfvénic. Note that the typical Alfvén speed in the low corona is over 600 km s^{-1} (Threlfall et al. 2013).

The apparent variation of the phase speed could also be connected with the variation of the polytropic index γ, and hence the effective sound speed with height in an isothermal and static plasma, caused by the misbalance of heating and cooling processes (Zavershinskii et al. 2019). A robust
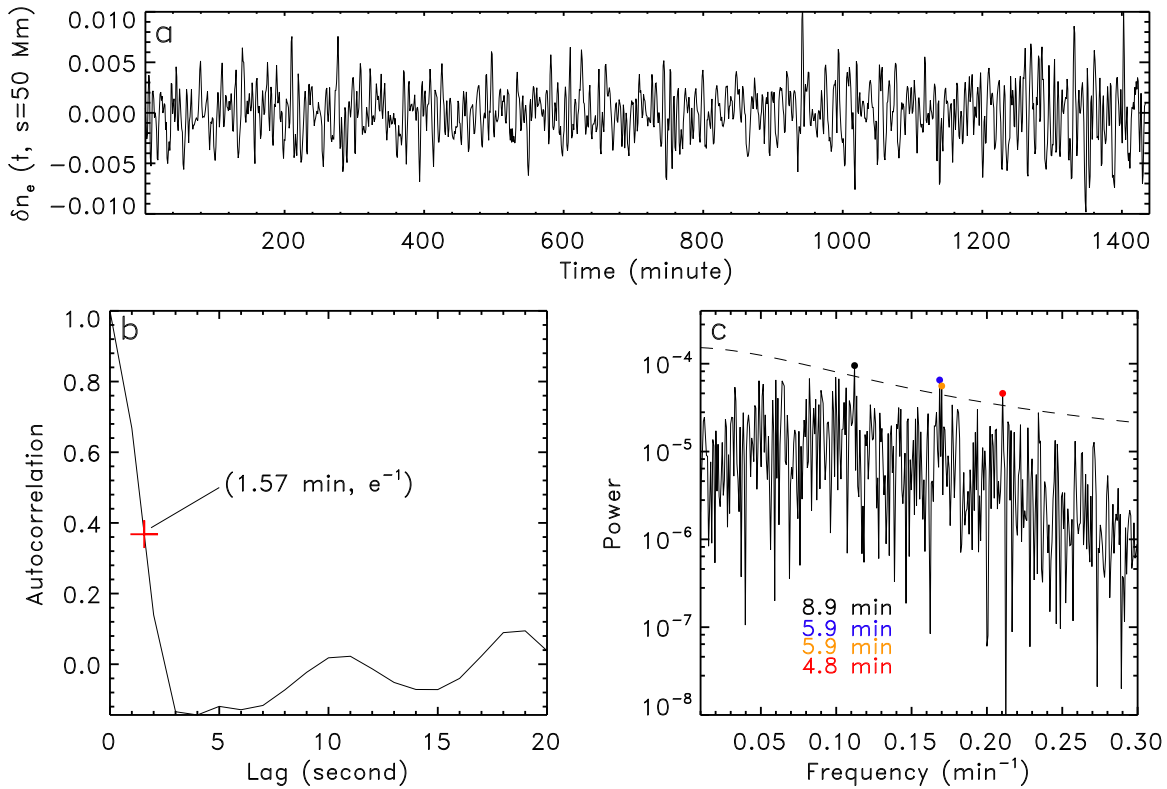
Figure 5. Perturbations of the electron number density at a distance of 50 Mm as indicated in Figure 3(a) (a), the corresponding autocorrelation (b), and the Fourier power (c). The red cross indicates the decorrelation time (*e*-folding time). The solid line in panel (c) represents 99.9% significance level of the red noise. Four colored circles represent the powers higher than the significance level. Their peak periods range from ∼5 to ∼9 minutes.

measurement of γ as a function of height would be helpful to examine the possibility, but such measurement seems only to be allowed on-disk where the signal-to-noise is high (e.g., Krishna Prasad et al. 2018). Coronal holes are possibly in nonequilibrium ionization (NEI) states (e.g., Bradshaw & Raymond 2013). It is shown that the measured plasma density and temperature could be affected by NEI in a rapidly heated system (e.g., Lee et al. 2019), while the NEI significantly affects the FIP and abundance in a coronal hole (Shi et al. 2019). Possible effects of NEI modulated by an MHD wave were explored through a forward modeling (Shi et al. 2019). An attempt to formulate MHD waves under an NEI condition have been performed only recently (Ballai 2019), which potentially could provide a tool for interpreting observations.

ORCID iDs

Il-Hyun Cho ⓘ https://orcid.org/0000-0001-7514-8171
Valery M. Nakariakov ⓘ https://orcid.org/0000-0001-6423-8286
Yong-Jae Moon ⓘ https://orcid.org/0000-0001-6216-6944
Jin-Yi Lee ⓘ https://orcid.org/0000-0001-6412-5556
Dae Jung Yu ⓘ https://orcid.org/0000-0003-1459-3057
Kyung-Suk Cho ⓘ https://orcid.org/0000-0003-2161-9606
Vasyl Yurchyshyn ⓘ https://orcid.org/0000-0001-9982-2175
Harim Lee ⓘ https://orcid.org/0000-0002-9300-8073

References

Ballai, I. 2019, FrASS, 6, 39
Banerjee, D., Gupta, G. R., & Teriaca, L. 2011, SSRv, 158, 267
Bemporad, A. 2017, ApJ, 846, 86
Bradshaw, S. J., & Raymond, J. 2013, SSRv, 178, 271
Caffau, E., Ludwig, H.-G., Steffen, M., et al. 2011, SoPh, 268, 255
Chen, Y., Feng, S. W., Li, B., et al. 2011, ApJ, 728, 147
Cho, I.-H., Cho, K.-S., Bong, S.-C., et al. 2017, ApJL, 837, L11
Cho, I.-H., Moon, Y.-J., Nakariakov, V. M., et al. 2018, PhRvL, 121, 075101
Cho, I.-H., Moon, Y.-J., Nakariakov, V. M., et al. 2019, ApJL, 871, L14
Cohen, O. 2011, MNRAS, 417, 2592
Decraemer, B., Zhukov, A. N., & Van Doorsselaere, T. 2020, ApJ, 893, 78
DeForest, C. E., & Gurman, J. B. 1998, ApJL, 501, L217
Deforest, C. E., Hoeksema, J. T., Gurman, J. B., et al. 1997, SoPh, 175, 393

DeForest, C. E., Howard, R. A., Velli, M., et al. 2018, ApJ, 862, 18
DeForest, C. E., Plunkett, S. P., & Andrews, M. D. 2001, ApJ, 546, 569
Feldman, U. 1992, PhyS, 46, 202
Feng, S. W., Chen, Y., Li, B., et al. 2011, SoPh, 272, 119
Gabriel, A. H., Bely-Dubau, F., & Lemaire, P. 2003, ApJ, 589, 623
Goossens, M., Hollweg, J. V., & Sakurai, T. 1992, SoPh, 138, 233
Griton, L., Pinto, R. F., Poirier, N., et al. 2020, ApJ, 893, 64
Gupta, G. R., Banerjee, D., Teriaca, L., et al. 2010, ApJ, 718, 11
Gupta, G. R., Teriaca, L., Marsch, E., et al. 2012, A&A, 546, A93
Krishna Prasad, S., Banerjee, D., & Gupta, G. R. 2011, A&A, 528, L4
Krishna Prasad, S., Banerjee, D., & Van Doorsselaere, T. 2014, ApJ, 789, 118
Krishna Prasad, S., Raes, J. O., Van Doorsselaere, T., et al. 2018, ApJ, 868, 149
Lee, J.-Y., Raymond, J. C., Reeves, K. K., et al. 2017, ApJ, 844, 3
Lee, J.-Y., Raymond, J. C., Reeves, K. K., et al. 2019, ApJ, 879, 111
Lemen, J. R., Title, A. M., Akin, D. J., et al. 2012, SoPh, 275, 17
McIntosh, S. W., Innes, D. E., de Pontieu, B., et al. 2010, A&A, 510, L2
Morgan, H., & Pickering, J. 2019, SoPh, 294, 135
Nakariakov, V. M. 2006, RSPTA, 364, 473
Nakariakov, V. M., Roberts, B., & Mann, G. 1996, A&A, 311, 311

Ofman, L., Nakariakov, V. M., & DeForest, C. E. 1999, ApJ, 514, 441
Ofman, L., Romoli, M., Poletto, G., et al. 1997, ApJL, 491, L111
Pesnell, W. D., Thompson, B. J., & Chamberlin, P. C. 2012, SoPh, 275, 3
Poletto, G. 2015, LRSP, 12, 7
Pucci, S., Poletto, G., Sterling, A. C., et al. 2014, ApJ, 793, 86
Samanta, T., Banerjee, D., & Tian, H. 2015, ApJ, 806, 172
Samanta, T., Tian, H., Yurchyshyn, V., et al. 2019, Sci, 366, 890
Saqri, J., Veronig, A. M., Heinemann, S. G., et al. 2020, SoPh, 295, 6
Schulz, M., & Mudelsee, M. 2002, CG, 28, 421
Shi, M., Li, B., Van Doorsselaere, T., et al. 2019, ApJ, 870, 99
Shi, T., Landi, E., & Manchester, W. 2019, ApJ, 882, 154
Telloni, D., Giordano, S., & Antonucci, E. 2019, ApJL, 881, L36
Teriaca, L., Poletto, G., Romoli, M., et al. 2003, ApJ, 588, 566
Threlfall, J., De Moortel, I., McIntosh, S. W., et al. 2013, A&A, 556, A124
Tian, H., DeLuca, E. E., Cranmer, S. R., et al. 2014, Sci, 346, 1255711
Tian, H., McIntosh, S. W., Habbal, S. R., et al. 2011, ApJ, 736, 130
Wang, T. J., Ofman, L., Davila, J. M., et al. 2009, A&A, 503, L25
Zavershinskii, D. I., Kolotkov, D. Y., Nakariakov, V. M., et al. 2019, PhPl, 26, 082113